NUCL SCI TECH (2016) 27:40
DOI 10.1007/s41365-016-0051-4

Characterization of solid particles sampled from condensates in boiling water reactor

Yu-Hung Shih[1] · Tung-Jen Wen[1] · Liang-Cheng Chen[1] · Tsuey-Lin Tsai[1]

Received: 2 June 2015 / Revised: 26 July 2015 / Accepted: 1 August 2015 / Published online: 11 April 2016

Abstract The growth, activation and deposition of corrosion products are the primary sources of radiation buildup on the surface of out-of-core piping in nuclear power plants. The buildup of radiation can have negative effects on the performance of the facility and cause harm to staff during maintenance outages for refueling. This paper reports on the crystalline and amorphous structures of corrosion products sampled in the boiling water reactors in nuclear power plants of Kuo-Sheng and identified using an acid dissolving technique. X-ray diffraction, scanning electron microprobe and inductively coupled plasma-atomic emission spectroscopy were used to analyze the samples. The results indicate that the quantity of amorphous iron oxide at inlet of the condensate demineralizer in Unit 2 is higher than that in Unit 1. The proportion of crystalline to amorphous corrosion products can affect the efficiency of removal. Thus, these results can be used to explain the difference in removal efficiency of condensate demineralizers in different units. Moreover, the iron oxide structures with various properties were observed in different operational periods. It is probable that the higher proportion of amorphous structures with a smaller particle size would reduce efficiency in the removal of condensate demineralization in Unit 2.

Keywords Boiling water reactor · Water chemistry · Iron · Corrosion product

✉ Yu-Hung Shih
yuhung0616@iner.gov.tw

[1] Chemistry Division, Institute of Nuclear Energy Research, Longtan, Taoyuan

1 Introduction

Kuo-Sheng Nuclear Power Station (KNPS) is a twin-unit boiling water reactor (BWR), located on the northern coast of Taiwan. Being a GE BWR-6 reactor (2943 MWth/985 MW), Unit 1 has been in operation since 1981, and Unit 2 since 1983. The hydrogen water chemistry (HWC) technique was implemented in 2006. The concentration of hydrogen in the final feedwater (FFW) is maintained at 1.0–1.1 ppm, which can typically reach the protection level lower than −230 mV (SHE) in operation (>10 % power) [1]. The addition of hydrogen into the feedwater system is an effective means of mitigating intergranular stress corrosion cracking (IGSCC) in austenitic stainless steel piping. A change in reactor water chemistry from normal water chemistry (NWC) to HWC leads to a change in the chemical environment from oxidizing to reducing, thereby reducing the rate at which cracks form. The implementation of HWC has two major side effects: an increase in main steam line radiation levels and intensity of the radiation field in the piping during operations [2, 3]. HWC involves injection of hydrogen gas into the BWR's feedwater. The hydrogen gas would suppress the oxygen produced in the core, hence the reduced probability of corrosion.

In a BWR, most of the radiation to which personnel are exposed during maintenance-related shutdowns can be attributed to corrosion products deposited on piping wall and accumulating in the low flow regions. Details related to the transport process in a BWR system have been outlined [4]. In a BWR, the buildup of radiation begins with neutron activation in corrosion products deposited on fuel surfaces from the system used to feedwater into the reactor water. Historically, water chemistry research was primarily

concerned with reducing exposure to radiation in BWRs. Considerable success in improving water quality has shifted the focus toward proactive measures with which to counteract predicted difficulties.

The objective of this study was to reduce exposure to radiation by reducing the iron concentrations in the feedwater on corrosion product reduction countermeasures of condensate demineralizers. The iron concentration in the feedwater depends on effectiveness of the condensate demineralizer system. Empirical studies, and computer modeling studies, have shown that maintaining the feedwater iron content within 0.5–1.0 ppb can be helpful to minimize the shutdown dose rate [5]. The first condensate demineralizer systems for the removal of iron from BWRs varied in their success. Most plants using filtration devices, including filter/demineralizers or prefilters installed in the upstream of deep beds, are able to maintain iron concentrations within the desired range.

The Kuo-Sheng plant uses the processes of air scrubbing and backwashing air scrubbing, instead of ultrasonic resin cleaners, for cleaning resin fines, and corrosion products which would be adsorbed to the resin surface. A more advanced resin cleaning system has recently been evaluated as an alternative to the conventional resin cleaning process. Various issues related to ion exchange, including the selection of divinylbenzene (DVB) resins to improve the efficiency of corrosion product removal, have yet to be entirely resolved. Increasing the efficiency of corrosion product removal requires the particle size and the morphology of the corrosion products to be tested using appropriate physical and chemical methods to identify the specific characteristics of corrosion products in specific units. Data related to oxide corrosion products, including composition, morphology and particle size distribution, can be used to maximize the efficiency of corrosion product removal by the condensate demineralizer.

2 Experimental

2.1 Samples and analysis

Samples of corrosion products were obtained from Units 1 and 2 of BWRs. The samples comprised corrosion products collected by cellulose particulate filters (47 mm diameter; 0.45 μm pore size) using an integrated filtration method. Insoluble corrosion products and radioactive transition metal species were collected from approximately 1000–2000 L of water drawn from cross-linked resin beds for iron removal situated at the condensate demineralizer inlet (CDI) and condensate demineralizer effluent (CDE), and from the final feedwater sampling port as well. The feedwater was cooled and depressurized before being passed through the filters.

Elemental analysis was performed using inductively coupled plasma-atomic emission spectroscopy (ICP-AES) and radioactivity of the samples was measured using gamma ray spectrometry. Scanning electron microscopy (SEM) was used to characterize the morphologies of the corrosion products, and X-ray powder diffraction (XRD) was used for phase determination.

2.2 SEM/EDS

Topography of crud was determined using an SEM (JEOL, JSM-6510), which has a fully integrated energy dispersive X-ray analysis system (EDS). Crud samples were collected on 8-mm^2 pieces of double-sided carbon conductive adhesive tape mounted on sample holders and then dried under an infrared lamp (250 W) for 1 h.

2.3 XRD

Crud analysis was performed using a Bruker's D8 Advance diffractometer operated at 40 kV and 40 mA with a ceramic X-ray tube with Cu target (wavelength 1.5418 Å). A vertical theta–theta goniometer of $-110° < 2\theta < 168°$ was controlled using stepper motors in conjunction with optical encoders providing the smallest selectable step size 0.001°. The scanning range was $2\theta = 30°$–$80°$ at a speed of 1°/min. Two exchangeable devices were used to detect scattered X-rays: (1) a NaI(Tl) scintillation counter with background of 0.3 cps and dynamic range up to 2×10^6; and (2) a LynxEYE compound silicon strip detector with lower background (<0.1 cps) and the same resolution but more than 150 times faster. Moreover, the LynxEYE detector has fluorescence suppression capability, which eliminates the need for secondary monochromators. A reference standard, Corundum (Al_2O_3, NIST SRM 1976a), was used for calibration of the equipment by bringing the diffraction angle to zero prior to sample measurement. The program TOPAS Spectra was used for comparing the sample and reference diffraction spectra (TOPAS spectra) to enable the identification of the fractions of various crystalline phases in the samples.

2.4 ICP-AES

The concentrations of Fe, Co, Cu, Ni, Cr, Zn, and Mn (elements commonly encountered in corrosion products) were detected using ICP-AES (Horiba JY Ultima 2 ICP-AES) and normalized to a total of 100 %.

2.5 Analytical flowchart

A flowchart outlining the proposed sampling and analysis method is presented in Fig. 1. The corrosion products were analyzed using a dissolution method. Insoluble iron oxides were obtained at each sampling point in the condensate and feedwater system. The crystalline phase of the corrosion products varied with water chemistry conditions in the BWR. The samples thus included mostly crystalline hematite, magnetite, goethite, lepidocrocite, and non-crystallite under NWC and HWC environments. At first we were to do quantitative and qualitative analysis with XRD. However, the iron-bearing phases were of a poor crystallite structure and could not usually be identified using XRD. Therefore, the crystalline and amorphous forms of iron oxides were separated using a dissolving method with an appropriate chemical solution. Following filtration, the insoluble oxide was re-dissolved in aqua regia and then analyzed again using ICP-AES [6, 7].

A series of experiments was conducted to determine reliability of the techniques used for identification of iron oxides in the condensate systems of the BWR. The experiments are outlined as follows:

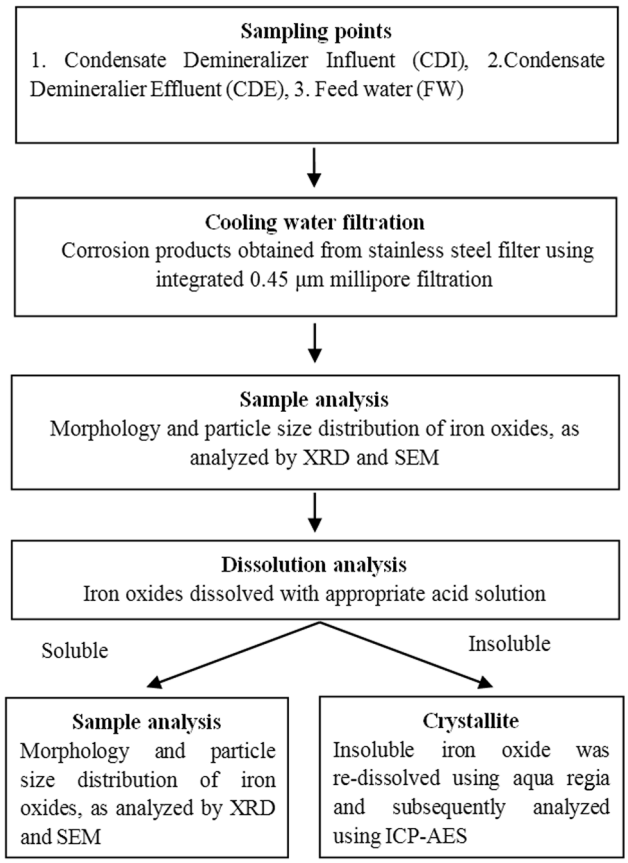

Fig. 1 Analytical flowchart of corrosion products

1. Iron oxide standards were tested using the proposed dissolving method (the specifics will be discussed later).
2. The Fe concentration was analyzed using ICP-AES.
3. The solubility of the iron oxide standard was calculated from the ICP-AES results.

Experiment data related to the proposed dissolution method are listed in Table 1. The experiment results clearly fit the expected values, indicating that the standard solubility of crystal iron oxides in the forms of hematite, magnetite, and goethite were lower than 2–7 %. However, the solubility of amorphous iron oxide and lepidocrocite exceeded 90 %. This indicates that the above pretests of crystallite and amorphous compositions in all samples can be calculated from the newly developed dissolution methods by the specific acid dissolution method.

3 Results and discussion

3.1 XRD analysis

Most of the piping used for the heater drain lines and condensate systems of BWRs are made of ferrous materials; therefore, the main component in the corrosion products is iron oxides. The corrosion products removed from different units were comparable in morphology and particle size distribution. All the iron oxides from both BWRs present the following crystallization shapes: γ-FeOOH, α-FeOOH, α-Fe_2O_3 and Fe_3O_4. Generally, quantitative analysis related to the shape of crystallites in iron oxides can be performed using FTIR [8], Mössbauer spectroscopy [9], or XRD analysis [10]. In our preliminary experiment, we performed qualitative analysis using XRD.

Figure 2 illustrates XRD patterns of three samples at different sampling points in Unit 1 operated under HWC. The XRD peak positions were calibrated against the standard using Bruker TOPAS software. This method reduced the error associated with quantitative analysis [11, 12]. Figures 3 and 4 present the fraction and relative concentrations of iron species in condensate influent, effluent and

Table 1 Solubility of iron oxides treated with proposed dissolution method

Iron oxide types	Test in chemical solution[a] (%)
Magnetite, Fe_3O_4	<7
Goethite , α-FeOOH	<2
Hematite, α-Fe_2O_3	<3
Lepidocrocite , γ-FeOOH	>90
Amorphous, $Fe(OH)_3$	>90

[a] Test in aqua regia: 90–100 %

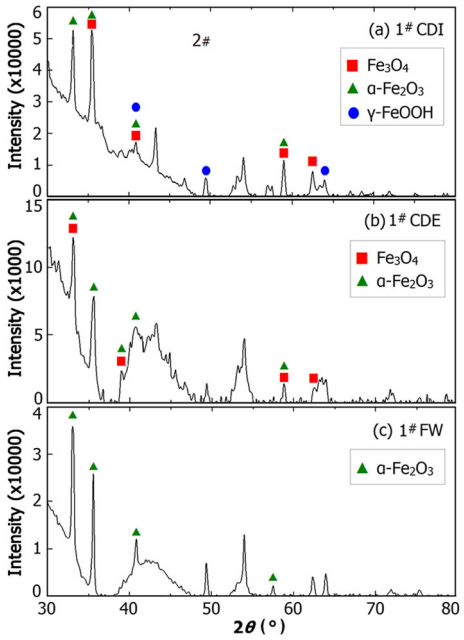

Fig. 2 XRD analysis of samples obtained at various sampling points in Unit 1 operated under HWC

feedwater in Units 1 and 2 operated under NWC or HWC conditions. Under both conditions, the concentrations of α-Fe_2O_3 (space group R3c, $a = 5.04$ Å, $c = 13.77$ Å of unit cell) was of the highest proportions. The condensate demineralizer produced the highest proportion of α-Fe_2O_3 under NWC conditions, but it was comparable in proportion under HWC condition. Significant differences in morphological composition of CDI were observed between Units 1 and 2 under NWC and HWC conditions.

The corrosion products formed in the condensate demineralizer and feedwater comprised mainly α-Fe_2O_3 (hematite). Hematite is a trigonal crystal structure, which is weakly anti-ferromagnetic at room temperature. Thermodynamic theory and experimental data indicate that the Fe^{3+} oxide phases of hematite and goethite structures are stable. The formation of hematite and goethite depends on the water temperature and pressure. Hematite forms under high temperatures, whereas goethite forms under high pressure. CDI temperatures are maintained at 30–40 °C, and corrosion products, such as α-FeOOH and α-Fe_2O_3, commonly form on the pipe walls. However, increasing the temperatures of FW within a pipeline to 200–240 °C tends

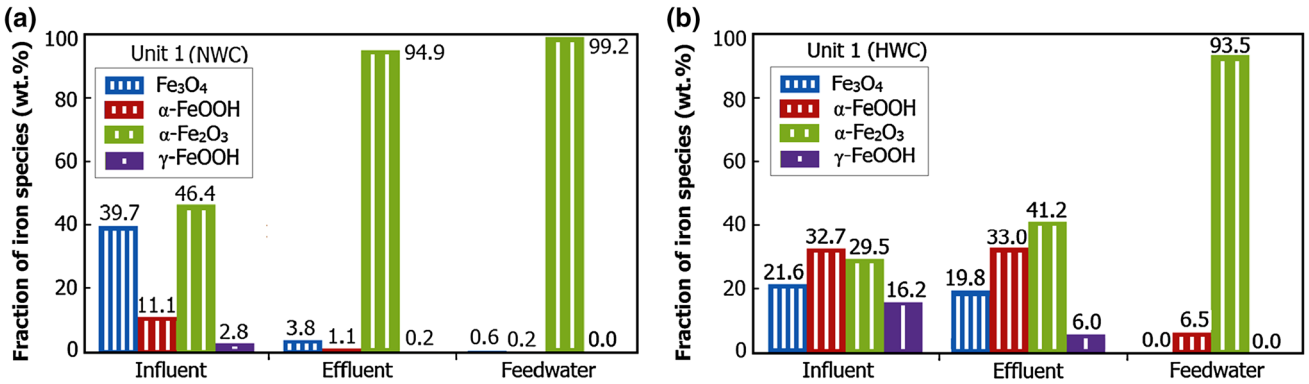

Fig. 3 Fraction of iron species from condensate influent, effluent and feedwater in Unit 1 operated in NWC (**a**) and HWC (**b**)

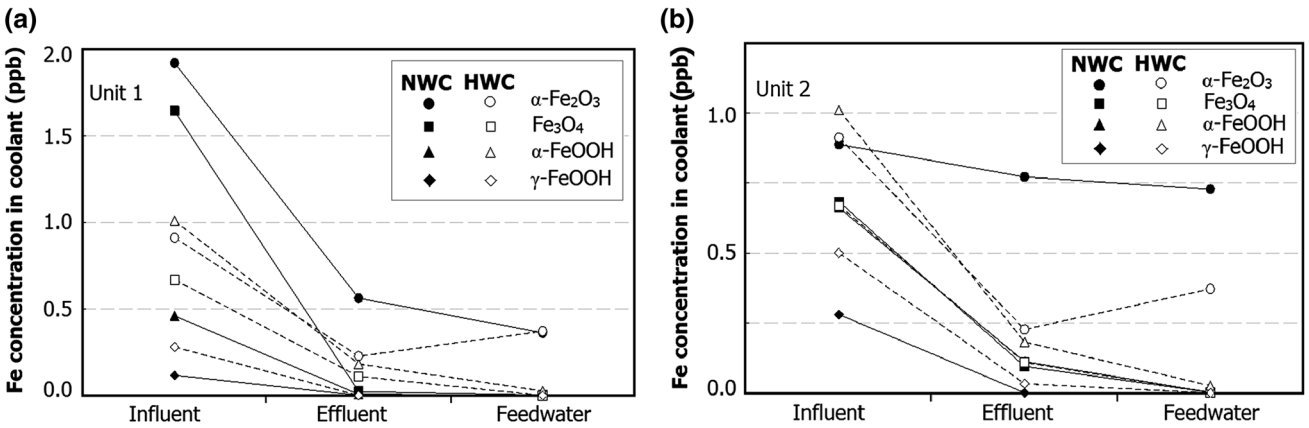

Fig. 4 Concentrations of iron species from influent, effluent, and final feedwater of Unit 1 (**a**) and Unit 2 (**b**)

Table 2 Results of crystallite and amorphous separation analysis (wt%) of corrosion products from CDI, CDE and FW

Conditions	Types	#1 CDI	#1 CDE	#1 FW	#2 CDI	#2 CDE	#2 FW
NWC	Crystallite Fe	39.9	19.6	42.4	35.6	14.3	36.4
	Amorphous Fe	60.1	80.4	57.6	64.4	85.7	63.6
HWC	Crystallite Fe	53.4	44.8	64.3	50.2	51.9	78.0
	Amorphous Fe	46.7	55.2	35.7	49.8	48.1	22.0

Table 3 Typical composition (in wt%) of iron oxide corrosion products in KNPS condensate

Operation conditions	Before 1993 (NWC)		April 2001 (NWC)		June 2012 (HWC)	
	Unit 1	Unit 2	Unit 1	Unit 2	Unit 1	Unit 2
Amorphous	28	42	26.6	30.8	46.6	49.8
Crystallite	72	58	73.4	69.2	53.4	50.2
Fe_3O_4	21	11	34.5	27	25	33
α-Fe_2O_3	21	12	–	5.5	27	45
α-FeOOH	9	16	–	4.5	33	17
γ-FeOOH	49	31	65.5	63	15	5

to cause the formation of α-Fe_2O_3. At higher temperatures, nearly all Fe in reactor water is an insoluble and stable form of α-Fe_2O_3. Kim indicated that extending the immersion time of oxide film on type 316 stainless steel in water at 288 °C was required to stabilize the potentials upon changing the water condition from NWC to HWC. This might have a slow transition rate of the α-Fe_2O_3 phase to Fe_3O_4 phase. Medium-level hydrogen injection has been in use for more than three years in the plants in this study. Thus, the reduction of α-Fe_2O_3 to Fe_3O_4 in pure water at 288 °C appears to be kinetically inhibited. This can be attributed to the fact that nearly all of the iron crud deposited on the outer cladding surface was in a fully oxidized state, α-Fe_2O_3 [13, 14].

Figure 3 indicates that the relative percentage of hematite increased rapidly in the FW under NWC and HWC conditions. Figure 4 shows that the relative percentages of goethite, lepidocrocite and magnetite in the FW were far lower than those obtained in the condensate. When coolant-borne iron particles pass through a resin bed, most of the large size crystalline is removed. Small residual particles transform into hematite under the high temperatures encountered in the FW.

3.2 Dissolution method and ICP-AES analysis

The samples for ICP-AES analysis were treated with a specific chemical solution to dissolve the iron oxides in the condensate system, and reliability of the treatment was studied with a series of experiments. Following treatment of the crud samples, the amorphous and crystalline structures were separated using a millipore filter. The procedures of dissolving the iron oxide and treating the samples are outlined as follows:

1. Add acidic reagents to the samples, disperse them ultrasonically, and heat them to a high temperature.
2. Samples are separated using a millipore filter at room temperature.
3. The filtrate is analyzed using ICP-AES.
4. The insoluble oxides are re-dissolved using aqua regia and are analyzed using ICP-AES; and
5. Calculate the ICP-AES data.

Table 2 lists the composition of corrosion products from Units 1 and 2. The amount of amorphous iron oxide in the CDI of Unit 2 is approximately 5 % higher than that observed in Unit 1 under the NWC and HWC conditions. Table 3 lists the typical composition of iron oxide corrosion products in KNPS condensate since 1993.

3.3 SEM and EDS analysis

The surface morphology, particle size, and composition of the iron oxide corrosion products were characterized by SEM (Fig. 5). The SEM images of the CDI and CDE samples reveal aggregates of very small dispersible particles (<2 μm) and elongated particles (>0.45 μm), while the corrosion products in the FW include small dense particles with a partial acicular structure. The large particles in the CDI could be removed from the cooling water by the condensate demineralizer. Between the CDE and FW, the cooling water temperature increases from 42 to 215 °C. Under these conditions, corrosion products in the form of small particles would be transformed into hematite

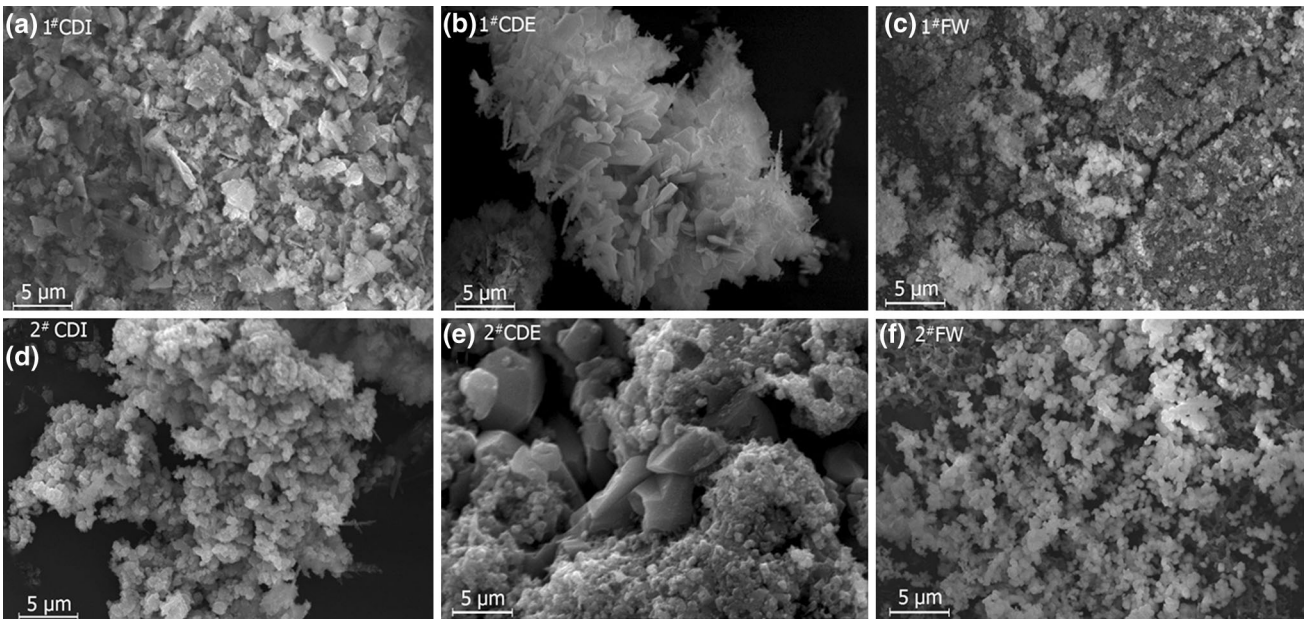

Fig. 5 (Color online) SEM images of corrosion product samples from the CDI, CDE, and FW in Units 1 and 2

structures. The SEM results indicate that the corrosion products from Units 1 and 2 had a similar crystalline structure except for the proportion of particle size. The samples obtained from the CDI of the HWC contain rhomboidal (α-Fe_2O_3), octahedral (Fe_3O_4) and acicular (α-FeOOH) particles, and a higher proportion of rhomboidal (α-Fe_2O_3) particles were generated in the CDE. Both the SEM and XRD results indicate that no significant change is occurred following a switch from NWC to HWC.

Figure 6 shows size distribution of the CDI corrosion products at Units 1 and 2. The small particles in Unit 2 are larger in number than in Unit 1. The size distributions of dispersible particles were as follows: CDI (0.45–1.5 μm), CDE (0.45–2.0 μm), and FW (0.45–1.0 μm).

The results of EDS analysis are listed in Table 4. The elemental compositions of samples obtained at the CDI, CDE, and FW of Unit 1 include mainly Fe, with minor amounts of Cu, Ni, and Mn. The source of the Cu, Ni, and Mn may be the materials used in the piping.

3.4 Removal efficiency of condensate demineralizer

Table 5 illustrates the removal efficiency of condensate demineralizer in Units 1 and 2. We used the direct data from KNPS operation and calculated results with the experimental data to obtain the removal efficiency. The removal efficiency of the condensate demineralizer in Unit 2 was 2–15 % lower than that of Unit 1 under NWC and HWC conditions. From Figs. 5 and 6, the particle size of the corrosion products in the CDI of Unit 2 is smaller than that of Unit 1. Such small particles are difficult to filter out

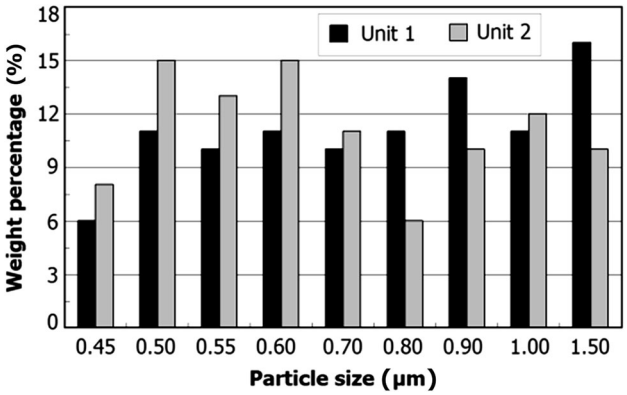

Fig. 6 Particle size distribution of corrosion products from the CDI in Units 1 and 2

using a condensate demineralizer. In addition, the quantity of amorphous iron oxide in the CDI of Unit 2 is higher than that in Unit 1, as shown in Table 2.

The removal efficiency of corrosion products depends primarily on the chemical form and particle size of the corrosion product intended for adsorption on the resin surfaces. Smaller particles pass easily through the condensate demineralizer, whereupon crystalline and amorphous structures adsorb on the cation exchange resins due to differences in zeta potential. At approximately pH 7, the corrosion products are positively charged, and the cation exchange resins are negatively charged. Thus, the corrosion products are adsorbed on the surface of the cation exchange resins by an attractive force. However, an amorphous structure has lower potential than does a

Table 4 Metal contents in corrosion product samples at the CDI, CDE, and FW of Units 1 and 2 under NWC/HWC conditions

Samples	Mn (wt%)		Fe (wt%)		Ni (wt%)		Cu (wt%)	
	Unit 1	Unit 2	Unit 1	Unit 2	Unit 1	Unit 2	Unit 1	Unit 2
CDI	–	1.3/0.4	90.8/94.6	83.4/91.8	–	4.6/1.2	9.3/4.8	10.7/6.6
CDE	–	–	97.6/93.7	96.6/93.7	–	–	2.47/6.3	3.4/6.4
FW	–	–	100/94.3	98.0/94.7	–	–	–/5.8	2.0/5.3

Table 5 Removal efficiency of corrosion products from condensate demineralizer at KNPS Units 1 and 2

Condition	Type	Unit 1 (%)	Unit 2 (%)
NWC	Crystallite Fe	94.5	79.0
	Amorphous Fe	77.7	70.6
	Total Fe	84.7	74.4
HWC	Crystallite Fe	80.3	82.0
	Amorphous Fe	88.4	79.5
	Total Fe	84.5	80.8

crystalline structure. As a result, the proportion of crystalline to amorphous material can affect the removal efficiency of corrosion products. It is probably that Unit 2 has a higher proportion of amorphous structures of smaller size, which resulted in lower removal efficiency than that observed in Unit 1. This could be explained by the fact that the removal efficiency of condensate demineralizer appears not to be influenced by whether the removal process occurs under NWC or HWC conditions.

4 Conclusion

This study developed a dissolving technique for the characterization of corrosion products and then the proposed method is applied to samples obtained from three sampling points in the KNPS: condensate influent, condensate effluent, and feedwater. We also compared the morphology of iron oxides from Units 1 and 2 of KNPS under NWC and HWC conditions. SEM results indicate that the morphology of corrosion products at Unit 2 (under NWC) is similar to that of Unit 1 (under HWC). The corrosion products obtained from feedwater showed a partial dense with particle sizes smaller than that observed in samples from the CDI and CDE. XRD patterns underwent quantitative as well as qualitative analysis, the results of which demonstrate that oxides of γ-FeOOH, α-FeOOH, α-Fe_2O_3, and Fe_3O_4 formed in the CDI, CDE and FW under NWC as well as HWC conditions. A higher proportion of α-Fe_2O_3 formed in the condensate demineralizer and feedwater. These results also showed that, in the FW, the concentration of α-Fe_2O_3 oxides increased due to the effects of higher temperature. Under the same conditions, the concentrations of Fe_3O_4, γ-FeOOH, and α-FeOOH oxides decreased. The results of the proposed dissolving method and ICP-AES analysis both indicate that the amount of amorphous iron oxide at the CDI in Unit 2 exceeds that in Unit 1. It is probable that a higher proportion of smaller, amorphous structures reduced the removal efficiency of the condensate demineralizer in Unit 2 to below that of Unit 1. Nonetheless, our data supports the conclusion that the morphology of iron oxides as well as the removal efficiency of the condensate demineralizers in all three sampling points was unaffected by the chemical conditions (i.e., NWC or HWC). However, it should be noted that other factors, such as flow rate through the deep-bed demineralizer or resin cross-linkage percent, would affect the removal efficiency of the condensate demineralizer. This report focuses on the structure and morphology of corrosion products, the results of which could enhance the ability to make predictions related to the removal efficiency of corrosion products as well as providing a reference for improving the quality of reactor water.

References

1. T.L. Tsai, T.Y. Su, T.Y. Wang et al., Characterization of crud deposited on fuel rods under HWC environment, in *Kuosheng nuclear power plant*. Nucl Sci Tech, accepted by Nuclear Science and Techniques (2015)
2. T.L. Tsai, T.Y. Lin, T.Y. Su et al., Chemical and radiochemical analysis of corrosion products on BWR fuel surfaces. J. Radioanal. Nucl. Chem. **295**, 289–296 (2013). doi:10.1007/s10967-012-1864-1
3. C.C. Lin, F.R. Smith, R.L. Cowan, Effects of hydrogen water chemistry on radiation field buildup in BWRs. Nucl. Eng. Des. **166**, 31–36 (1996). doi:10.1016/0029-5493(96)01196-X
4. C.C. Lin, A review of corrosion product transport and radiation field buildup in boiling water reactors. Prog. Nucl. Energy **51**, 207–224 (2009). doi:10.1016/j.pnucene.2008.05.005
5. U. Shunsuke, A. Yamato, K. Masao et al., Estimation of shutdown dose rate around recirculation pipes during operating life of boiling water reactors. J. Nucl. Sci. Technol. **17**, 119–128 (1980). doi:10.1080/18811248.1980.9732555
6. T. Misawa, Corrosion morphologies and products of iron and steels in the wet corrosion. Bull. Jpn. Inst. Metals **20**, 201–210 (1985). doi:10.2320/materia1962.24.201
7. R.M. Cornell, U. Schwertmann, *The Iron Oxides in the Laboratory* (VCH Publishers, Germany, 1991). doi:10.1097/00010694-199311000-00012

8. A. Raman, B. Kuban, Infrared spectroscopic analysis of phase transformation process in rust layers formed on weathering steel in bridge spans. Corros. Rng. **44**, 483–488 (1988). doi:10.5006/1.3583966
9. J.A. Sawicki, Analyses of crud deposits on fuel rods in PWRs using Mössbauer spectroscopy. J. Nucl. Mater. **402**, 124–129 (2010). doi:10.1016/j.jnucmat.2010.05.007
10. K. Baberschke, X-ray magnetic dichroism the technique of choice to study magnetism element specifically. Phys Scr (2005). doi:10.1238/Physica.Topical.115a00049
11. A. Jerzy, Analyses of fuel crud and coolant-borne corrosion products in normal water chemistry BWRs. J. Nucl. Mater. **419**, 85–96 (2011). doi:10.1016/j.jnucmat.2011.08.032
12. F.H. Ruddy, A.R. Dulloo, J.G. Seidel et al., The charged particle response of silicon carbide semiconductor radiation detector. Nucl. Instrum. Methods Phys. Res. **505**, 159–162 (2003). doi:10.1016/S0168-9002(03)01041-6
13. Y.J. Kim, Characterization of the oxide film formed on type 316 stainless steel in 288 °C water in cyclic normal and hydrogen water chemistries. Corros. Sci. **51**, 849–860 (1995). doi:10.5006/1.3293562
14. U. Schwertmann, R.M. Cornell, *The Iron Oxides, Iron Oxides in the Laboratory* (VCH Publishers, Germany, 2000). doi:10.1002/9783527613229.ch01